Controlled Hydrogenation of Graphene Sheets and Nanoribbons

Manu Jaiswal,[†,‡] Candy Haley Yi Xuan Lim,[†] Qiaoliang Bao,[†] Chee Tat Toh,[‡] Kian Ping Loh,*[,†] and Barbaros Özyilmaz*[,‡,§,⊥]

[†]Department of Chemistry, 3 Science Drive 3, and [‡]Department of Physics, 2 Science Drive 3, National University of Singapore, Singapore 117542, [§]Nanocore, 4 Engineering Drive 3, National University of Singapore, Singapore 117576, and [⊥]Graduate School for Integrative Sciences and Engineering (NGS), National University of Singapore, Singapore 117456

ABSTRACT The electronic properties of graphene sheets and nanoribbons with different degrees of hydrogenation have been investigated using a combination of charge transport and Raman spectroscopy experiments. The field-effect transistor mobility of graphene is shown to be highly sensitive to the treatment time during atomic hydrogen dose and follows an exponential decrease with time. Raman spectroscopy demonstrates linearly increasing defect-band intensity, and when considered together with transport data, the relationship between graphene mobility and the crystalline size of intact sp^2 carbon regions can be derived. Further, the increase in width of the voltage plateau for monolayer and bilayer graphene points to the formation of midgap states. For partially hydrogenated graphene, the temperature-dependent transport in these states shows a weak insulating behavior. A comparison of Raman spectrum and conductivity data of partially hydrogenated monolayer and bilayer graphene suggests that the latter is also quite susceptible to adsorption of hydrogen atoms, despite a stiffer lattice structure.

KEYWORDS: graphene · hydrogenation · electronic properties · Raman spectroscopy

Chemical modification of the graphene surface is emerging as a useful tool to engineer new electronic properties. Among such modifications include covalent as well as noncovalent functionalization of graphene surfaces with organic molecules to achieve surface-transfer doping or band gap opening.[1] A band gap can be introduced in the highly conducting semimetallic graphene upon chemisorption of atomic hydrogen,[2] and this was experimentally demonstrated recently.[3] Addition of hydrogen atoms to the carbon scaffold results in the formation of covalent bonds with the p_z orbital of the carbon atom and modifies the band structure of the two-dimensional system. This discovery opens the possibility of having a promising new class of electronic devices with properties which are potentially tunable between ballistic transport to localized insulators. All-graphene circuits have been proposed that may simplify industrial processing, and such future circuit components may comprise of graphene electrodes and nanographene active material, whereas hydrogenated graphene can be potentially used to isolate individual transistors. The possibility of using hydrogenation to fabricate quantum dots and heterojunctions has been suggested; in particular, this may not require cutting or etching steps.[4] Favorable thermoelectric properties of ultrathin graphene nanoribbons (GNRs) have been predicted upon hydrogenation.[5] The extent of adatom adsorption may impact critically on physical phenomenon, such as the ferromagnetic state,[6−8] high-Tc superconductivity in the doped state,[9] spin−orbit coupling,[10] and Anderson localized insulator.[11]

Whereas the potential of hydrogenated graphene in electronic applications has been demonstrated, the dependence of electronic properties on the fraction of adsorbed hydrogen atoms has not been investigated in detail. The influence of short-range scatterers, such as chemisorbed adatoms, on the graphene mobility has been a subject of debate, and some early theoretical work assigned a density-independent form to all short-range scattering, while the mobility of graphene was assumed to depend entirely on charge impurity scattering from the underlying substrate.[12,13] From a theoretical point of view, a full Born approximation was assumed for all short-range scattering, and it is this assumption that has been questioned.[13−15] Lately, it has been argued that short-range scatterer, like adatoms, vacancies can actually mimic the influence of charged impurities and also contribute to a conductivity that is linear in density (up to logarithmic corrections).[15] This is further supported by a recent experiment, which has shown the presence of a tiny defect peak in the Raman spectrum of high-mobility graphene, pointing to the presence of adatoms in pristine

*Address correspondence to phyob@nus.edu.sg, chmlohkp@nus.edu.sg.

Received for review August 14, 2010 and accepted January 14, 2011.

Published online January 28, 2011
10.1021/nn102034y

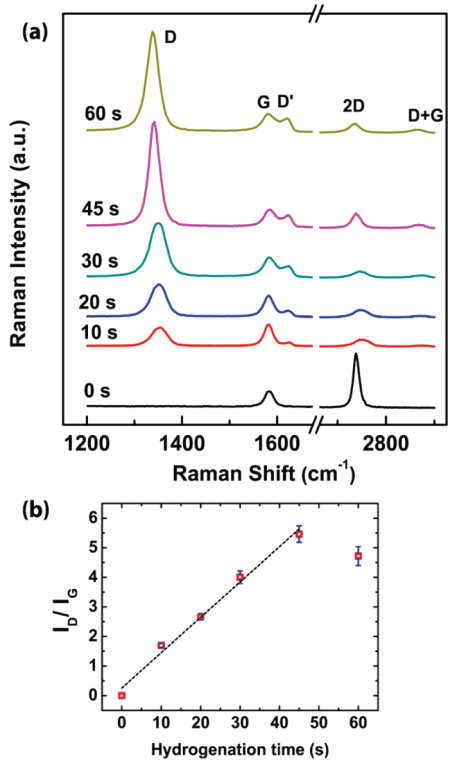

Figure 1. (a) Raman spectra of monolayer graphene taken for increasing exposure time (0−60 s) to hydrogen plasma. Additional peaks are observed with addition of hydrogen atoms as described in text. (b) Integrated D and G band intensity ratio (I_D/I_G) of monolayer graphene for increasing time exposure to hydrogen plasma (0−60 s).

graphene.[16] The exact quantitative role of remnant adatoms in pristine graphene is still being debated,[17] and experiments involving high doping of graphene indicate that short-range scattering in the weak scattering limit may not be entirely absent.[18] The chemical nature and precise density of adatoms in pristine graphene have not been measured directly yet, although it is increasingly evident that they play an important role in limiting the mobility of pristine graphene. In this work, we describe in detail the influence of controlled introduction of hydrogen adatoms on the charge transport properties of mono- and bilayer graphene and on GNRs. The formation of midgap states is another consequence of hydrogen adatoms, and the temperature-dependent measurements are used to characterize the transport in these states.

RESULTS AND DISCUSSION

Graphene flakes were subject to varying dose of hydrogen plasma, and their Raman spectrum was recorded. The evolution of the Raman spectra of monolayer graphene measured for different exposure times to hydrogen plasma is shown in Figure 1a. Pristine graphene spectrum has two prominent peaks: (1) G-peak at 1580 cm^{-1} corresponding to the in-plane bond-stretching optical vibrations of sp^2 carbon atoms and (2) 2D peak at 2680 cm^{-1} that exhibits a full width at half-maximum (fwhm) of ~27 cm^{-1}, the typical characteristic of monolayer graphene. The hydrogen treatment produces pronounced new features in the spectrum, which includes the formation of three new peaks at 1340, 1620, and 2920 cm^{-1}, as shown previously.[3,19] In particular, there is continuous enhancement in the D-peak (at 1340 cm^{-1}) with hydrogenation time which corresponds to defect formation upon the attachment of hydrogen atoms to the carbon lattice leading to intervalley scattering.[20] In addition, the 2D peak is strongly suppressed upon hydrogenation. The frequency-integrated G-band intensity is robust to the influence of external parameters and is often used as a reference to study the evolution of other peak intensities. The evolution of D- and G-band intensity ratio I_D/I_G is plotted in Figure 1b. This ratio shows a linear increase for $t < 45$ s hydrogenation time, beyond which it shows a tendency to decrease. The Raman intensity of the D-band, normalized to the G-band, has been used to estimate the crystallite size L_a on the surface of any thin graphite-like material, $L_a \propto (I_D/I_G)^{-1}$.[21−23] In the context of the hydrogenation experiment, this length scale can be associated with a localization length scale or the mean free path (depending on the nature of transport). The change in Raman intensity suggests a localization radius inversely proportional to the exposure time.

The Raman maps of integrated G-, D-, and 2D-band intensities for graphene flakes exposed to 10 s hydrogen plasma show distinct contrast for the number of graphene layers (see Figure 2a−d). Defect density and signal attenuation are the two factors that determine Raman intensity of defect band. The Raman signal probes the defect density on the top graphene surface, and the signal from defects is attenuated in the case of few-layer graphene due to the presence of intact sublayers. For the same level of defects induced in the top surface, the integrated I_D/I_G ratio in bilayer graphene is lower by an attenuation factor of ~3.5, when compared to monolayer graphene.[24] Therefore, the significantly higher I_D/I_G ratio (~ 1.7) in monolayer graphene is indicative of an even lower fraction of defects when compared to the case for bilayer graphene (see Supporting Information, S1).

Graphene samples chosen for investigation for study of electronic properties included the following: (1) bulk graphene sheets, (2) isolated GNR, and (3) parallel GNRs (see Methods Section for details of sample fabrication and Supporting Information, S2, for device structure). The resistance of a graphene flake is plotted as a function of back-gate voltage for increasing hydrogen plasma exposure (0, 5, 10, and 15s) in Figure 3a (dashed black line). The origin of the voltage axis is shifted to the conductivity minimum for ease of comparison between the different curves. It has been recently predicted from first-principles density functional theory (DFT) that a possible narrowing of the ribbons can be obtained upon partial hydrogenation, and enhanced evidence of edge reactivity is also known

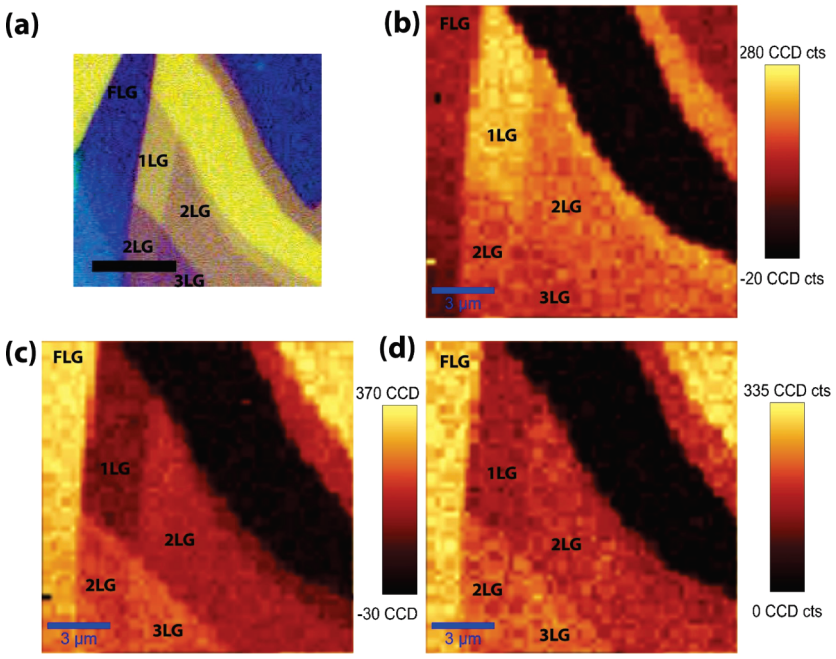

Figure 2. Graphene flakes exposed to 10 s hydrogen plasma. (a) Optical micrograph of mechanically exfoliated graphene showing graphene flakes of different thickness (color enhanced for clarity). (b) Raman map of integrated D-line intensity of the same region showing contrast in defect-induced signal in monolayer (1LG) graphene in comparison to bilayer (2LG) and trilayer graphene (3LG). (c) Raman map of integrated G-line intensity. (d) Raman map of integrated 2D line intensity. The Raman signal in monolayer probes the defect density on the top hydrogenated graphene surface, whereas this signal is attenuated in case of few-layer graphene due to an additional signal from intact sublayers. The stronger signal from the monolayer graphene is primarily a result of this attenuation process.

from the growth of metal oxides on graphene.[25] Therefore we considered the controlled hydrogenation of GNR structures. The resistance of isolated GNR is plotted as a function of back-gate voltage in Figure 3b. For a better comparison, parallel 100 nm GNRs and bulk graphene four-terminal devices are made on adjacent portions of the same graphene flake, and the modulation of resistance with back-gate voltage for both is plotted together in Figure 3a. Both parallel GNRs and bulk graphene show comparable modulation of transport properties upon hydrogenation. For the estimation of parallel GNR mobility, we also included the influence of fringe fields. These fringe fields are particularly important for isolated GNR since they result in a higher charge carrier density near the edges.[26] In case of several parallel GNRs, the influence of fringe fields is significantly reduced (see simulated values in Figure S6, Supporting Information). For parallel GNRs, the general trend of exponentially decaying mobility with increasing time exposure to hydrogenation remains similar to that of bulk graphene.

The conductivity of partially hydrogenated graphene shows close to linear dependence on carrier density away from the neutrality point (see Supporting Information, S3), and this is consistent with recent theoretical estimates on short-range scattering.[13] The field-effect mobility of the devices is estimated from the derivative of resistance *vs* back-gate voltage curves, $\mu_{FE} = (1/e)(\partial\sigma/\partial n)$, away from the neutrality point. A rapid decrease in the mobility is observed during $t < 5$ s exposure to the hydrogen plasma, due to the sensitivity of graphene sheet to adsorbed impurities (Figure 3c). Similar changes in electronic properties of graphene sheet and parallel GNRs are observed upon adsorption of hydrogen. Upon progressive hydrogenation, the time evolution of graphene mobility is well described by the empirical functional form: $\mu_{FE}(t) = \mu_0 \exp(-t/\tau) + \mu_\infty$, where $\mu_{FE}(t)$ is the mobility at time t, τ is a characteristic time that depends on the density of atoms and radicals in the hydrogen plasma, the rate of carbon−hydrogen bond formation, the hydrogenation barriers *etc.*, and μ_∞ is a residual mobility in the limit of large adsorption (Figure 3c). While this dependence is obtained experimentally, a correlation of these changes with theoretical predictions can be quite useful. Recently, the evolution of graphene conductance upon single-sided partial hydrogenation has been theoretically studied within the tight-binding approximation using transmission matrix coefficients.[27] At low density of adsorbates, the density of states is not affected, with the exception of sharp peaks at the charge neutrality point, representing midgap states.[15] In the region of high energy, variation of conductance with energy is independent of the subtle details of hydrogen adsorption process (*i.e.*, same sublattice *vs* both sublattice adsorptions). The signature of localization is significant near the neutrality point, but conductances at high-energy propagating channels continue to be "graphene-like".[27] A quantitative study of the former

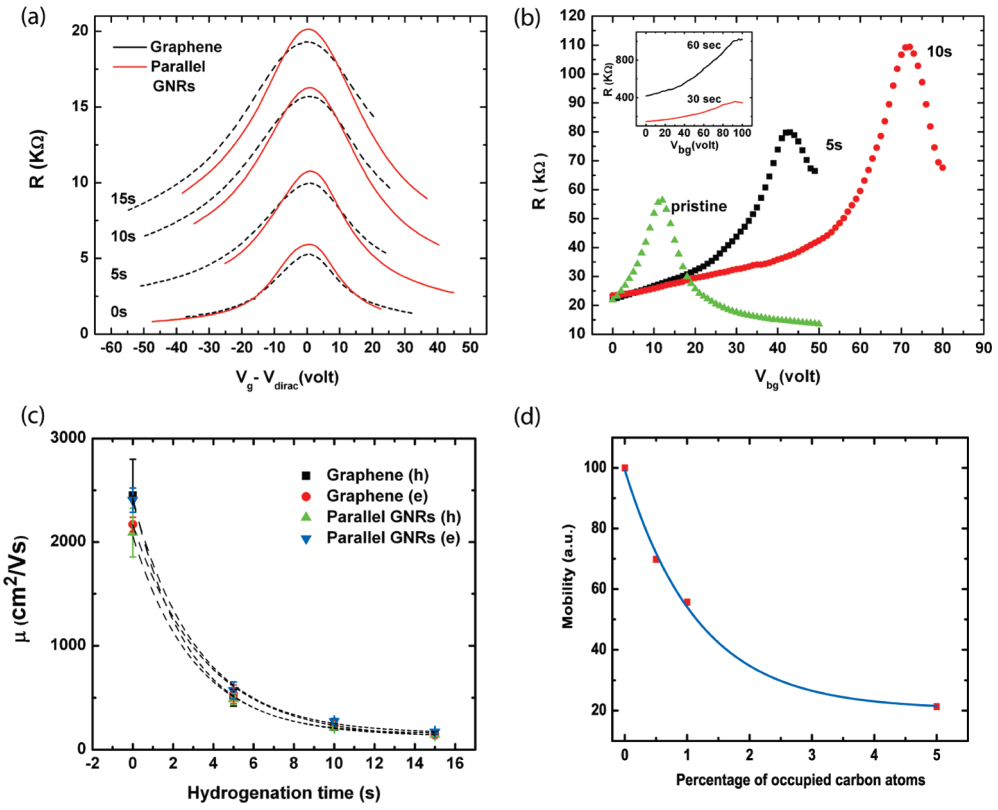

Figure 3. (a) Resistance (*R*) *vs* $V_{bg} - V_{dirac}$ with increasing hydrogenation time (0, 5, 10, and 15s) for a graphene sheet M1 (dashed black line) and parallel GNRs (red line); (b) *R vs* back gate (V_{bg}) with increasing hydrogenation time (0, 5, and 10s) for an isolated 100 nm GNR [Inset: *R vs* V_{bg} for longer exposure to hydrogen plasma (30 and 60s)]; (c) μ_e and μ_h *vs* hydrogenation time for graphene sheet and 100 nm parallel GNRs. Dashed lines are fits to exponential equation described in text; and (d) mobility (au) *vs* percentage of hydrogenated carbon atoms using data extracted from numerical computation work of ref 27. Dashed line is the exponential decay fit, with decay constant, $n_H^c \sim 1.17\%$.

requires very low temperatures to observe the conductance fluctuations, since thermal effects smear the sharp peaks in the density of states (DOS) near the neutrality point. On the other hand, the mobility measured away from neutrality point reflects the transport in the graphene-like channels, and it can serve as a suitable parameter for estimating the degree of hydrogen adsorption. This theoretical dependence of mobility on the fraction of hydrogenated carbon atoms is extracted from the numerical work of ref 27 and plotted in Figure 3d for comparison. The theoretical mobility of partially hydrogenated graphene (normalized to mobility of pristine graphene) is estimated from linear−fit to the conductance−carrier density plots of ref 27 (see Supporting Information, S4) in the energy region $E(k) = 0.7-1.6$ eV, measured from the neutrality *K*-point, using the expression, $\mu = \Delta\sigma/e\cdot\Delta n$. In this expression, the carrier density can be approximated by $\Delta n = \int_{E\text{-lower}}^{E\text{-upper}} D(E)d(E) \propto \Delta(E^2)$, since the DOS $D(E)$ shows only small deviations from the profile for pristine graphene for this energy bandwidth in the case of partial hydrogenation with fraction of hydrogenated carbon atoms not exceeding 5%. This change in mobility upon addition of hydrogen atoms to graphene is well described by the exponential decay functional form: $\mu_{FE}(n_H) = \mu_0 \exp(-n_H/n_H^c) + \mu_{sat}$, where n_H^c is the decay constant of this exponential fit to the data.

Since both the experimental curve of $\mu_{FE}(t)$ and the theoretically estimated dependence $\mu_{FE}(n_H)$ follow the exponential form, a linear process of hydrogenation can be inferred. In fact, the evolution of D- and G-band intensity ratio I_D/I_G in the Raman spectra also follows a linear trend for the initial time-dependent hydrogenation process (Figure 1b). This allows a direct computation of the fraction of impurity atoms on the carbon scaffold from the changes in field-effect mobility of graphene. The value of τ obtained for graphene sheet is 2.73 s (hole) and 3.51 s (electron) and for 100 nm parallel graphene ribbons 3.07 s (hole) and 3.18 s (electron). The exponential decay constant for the fit to $\mu(n_H)$ data (from fitted blue curve in Figure 3d) is $n_H^c \sim 1.17\%$ hydrogenated carbon atoms. A comparison of the two decay constants suggests that for $t = 10$ s of exposure, the mobility decreases by 90% from the value for pristine graphene, when approximately 3.4% of the carbon atoms are hydrogenated at this exposure, for the present experimental plasma conditions. Since hydrogenation is predicted to involve significant clustering of adatoms; the actual impurity separation relevant to transport will be much larger. When hydrogen atoms are adsorbed on graphene lattice, nanocrystalline regions of sp^2-bonded graphene (representing the nonhydrogenated portions) are formed between these

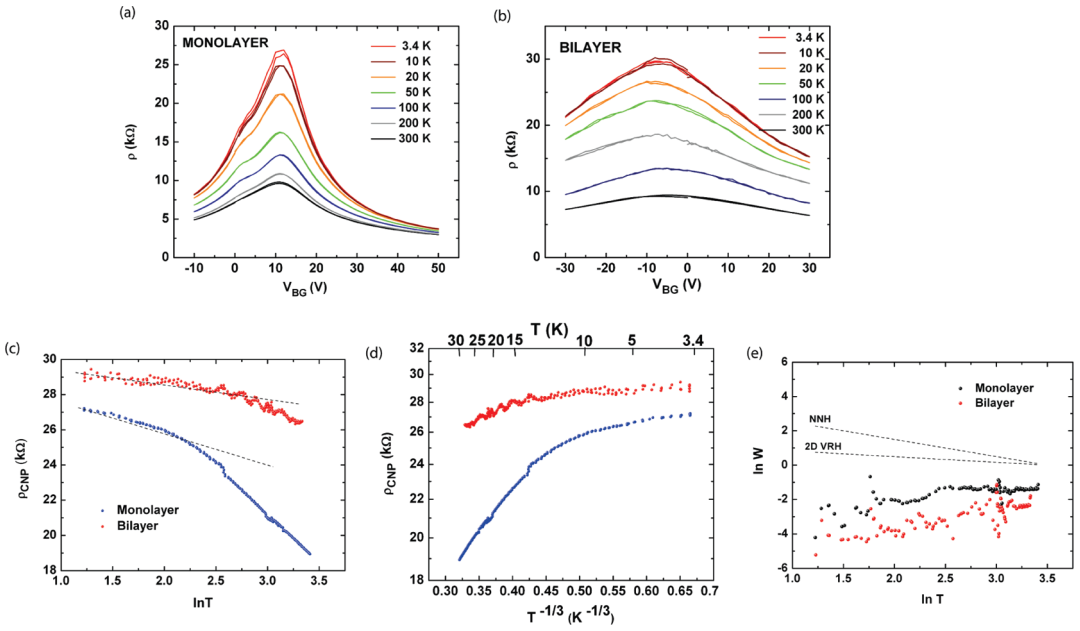

Figure 4. (a) Resistivity (R) *vs* V_{BG} for partially hydrogenated (t = 10 s) monolayer graphene sample M2, as a function of temperature in the range 3−300 K; (b) R *vs* V_{BG} for partially hydrogenated (t = 10 s) bilayer graphene sample B2, as a function of temperature in the range 3−300 K; (c) ρ_{CNP} *vs* ln(T) for monolayer graphene (blue) and bilayer graphene (red) between T = 3−30 K; (d) ρ_{CNP} (on log scale) *vs* $T^{-1/3}$ for monolayer graphene (blue) and bilayer graphene (red) between T = 3−30 K; and (e) reduced activation energy plot: ln W *vs* ln T for the same samples, gated at CNP. Dashed lines show expected exponent for hopping transport.

introduced defects. The size of these regions was obtained above using Raman spectroscopy. Upon combining the transport and Raman measurements, it follows that field-effect mobility decreases rapidly with a decrease in the size of crystalline regions upon the incorporation of hydrogen atoms, $\mu_{FE} \propto \exp(-k/L_a) \sim (1 - k/L_a)$, where k is a constant and L_a is the size of crystalline regions formed after the incorporation of defects. This observed decrease in the mobility with increasing hydrogenation is consistent with recent theoretical and experimental work, which suggests that hydrogen adatoms behave as resonant scatterers.[15,16] The influence of hydrogen atoms on the transport characteristics is two-fold: (1) the mobility of graphene decreases upon incorporation of hydrogen atoms and (2) the band structure is modified with the formation of additional states ("mid-gap states") near the charge neutrality point (CNP). These phenomena are discussed in detail for mono- and bilayer graphene in the following sections.

We now examine the nature of charge transport in partially hydrogenated graphene. The resistivity of partially hydrogenated (t = 10 s) mono- and bilayer graphene is plotted as a function of gate voltage at different temperatures in Figure 4. Across all charge carrier densities, the resistivity shows an insulating behavior at low temperature, $d\rho/dT < 0$ and can be attributed to enhanced intervalley scattering[20] from the short-range potential of hydrogen adatoms and the formation of midgap states near the neutrality point. The insulating behavior is more pronounced at low density, in the vicinity of the charge neutrality point. These transport characteristics of partially hydrogenated samples are remarkably different from that of pristine samples: Pristine monolayer graphene shows a temperature-independent transport particularly near the CNP, whereas pristine bilayer graphene shows an insulating behavior only in the vicinity of the CNP.[28] The resistivity at the neutrality point, ρ_{CNP}, is plotted as a function of temperature in the range 3−30 K in Figure 4c and d, showing the weak insulating behavior in these localized states. Previous investigations on hydrogenated monolayer graphene[3] and heavily ozonated monolayer graphene[29] have described the temperature dependence of resistivity near the CNP within the two-dimensional variable range-hopping (VRH) framework, indicating strong localization. Further, a transition to weak localization is suggested both at high densities and/or at high temperatures.[29] In comparison to the samples in ref 3, the temperature dependence near CNP in our partially hydrogenated samples is weaker, even though the Raman spectrum indicates a comparable defect density. This difference may indicate that the nature of localization not only depends on the defect concentration but also on other factors, such as clustering of defects, rippling of graphene, *etc*. Investigation of the reduced activation energy, $W(T) = -d \ln R/d \ln T$, on the double logarithmic scale allows us to distinguish various electron transport laws for disordered systems using the method of Zabrodskii *et al*.[30,31] This is plotted in Figure 4e for the CNP. A comparison with the hopping exponents shows that the transport in the vicinity of CNP for partially hydrogenated

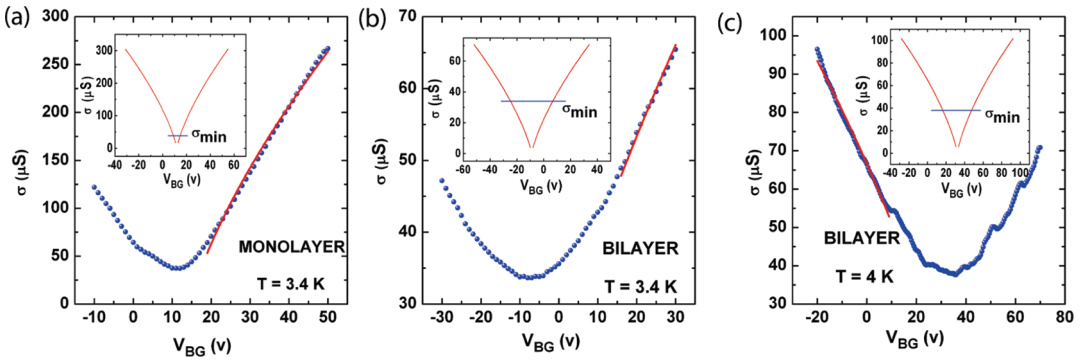

Figure 5. Conductivity *vs* V_{BG} for: (a) partially hydrogenated (t = 10 s) monolayer graphene sample M2 at T = 3.4 K; (b) partially hydrogenated (t = 10 s) bilayer graphene sample B2 at T = 3.4 K; and (c) partially hydrogenated (t = 10 s) bilayer graphene B1 at T = 4 K. For all three samples, the red line represents a single-parameter fit to resonant scatterer (RS) induced conductivity. (Insets: Intersection of simulated RS conductivity and experimentally measured σ_{min}, giving the width of voltage plateau: ΔVg = 6, 32.4, and 31.2 V for samples M2, B2, and B1, respectively).

monolayer and bilayer graphene is clearly distinct from hopping type, and the system is close to the critical regime. In our samples, the temperature dependence of resistivity, even at CNP, is rather weak, and the differences in the nature of localization with the previous works (ref 3 and 29) are most obvious in the reduced activation energy plot (Figure 4e). It is likely that the system is closer to the weak localization scenario, although it clearly shows deviations from the exact form of weak localization for a two-dimensional electron gas (2DEG) (Figure 4c). Finally, the slope of the VRH plot of ρ(T) for BLG (Figure 4d) gives a value of localization length, $\xi_{VRH} > 1$ μm. This value is much larger than the typical estimates for the phase coherence length, as discussed below. This partially hydrogenated graphene offers a platform to test theoretical models for adatom scattering, since they are expected to dominate the transport.

We next examine the broadening of the width of voltage plateau near the CNP, upon exposure to hydrogen atoms. As shown in Figure 3a for monolayer graphene, the width of voltage plateau is enhanced with increasing exposure to hydrogen plasma. While comparable changes are observed across several samples at room temperature (see Supporting Information, S9), representative samples partially hydrogenated to 10 s were measured at low temperature, and the results are plotted in Figure 5. For monolayer graphene, the conductivity induced by resonant scatterers is described by the equation:[32]

$$\sigma = \frac{4e^2}{h}\frac{{k_F}^2}{2\pi n_i}\ln^2(k_F R) \qquad (1)$$

where $k_F = (\pi n)^{1/2}$ is the Fermi wave vector, n_i is the concentration of hydrogen atoms, and R is the impurity radius. Since scattering is expected to be dominated entirely by hydrogen adatoms, we use the above equation to fit the σ *vs* V_{BG} data at T = 3.4 K. Assuming $R \sim 1$ Å as the size of impurity potential, a single-parameter fit to this equation gives a value of impurity density, $n_i \sim 3 \times 10^{12}$/cm^2. This value is significantly higher than typical values obtained for pristine monolayer graphene ($\sim 2.5 \times 10^{11}$/cm^2)[32] and reflects the influence of hydrogen atoms. The width of the voltage plateau ($\Delta V_g \approx 6$ V) is obtained from the intersection of the experimentally measured conductivity minima (σ_{min}) and the conductivity curve simulated using the above value of R, n_i (see inset of Figure 5a). This width represents the hydrogen adatom induced modification of graphene band structure, *i.e.*, the formation of midgap states. For the case of partially hydrogenated bilayer graphene, the applicability of linear or sublinear dependence of conductivity on carrier density depends on the energy interval. Disordered samples can be expected to follow a trend similar to that of monolayer graphene, since the presence of a wider bandwidth of midgap states may not allow the observation of linear dependence.[32,33] In a recent experiment on scattering in bilayer graphene, the density dependence of conductivity was described entirely by a sublinear form arising from resonant scatterers, although the nature of these scatterers (possibly adatoms) was not known, since their introduction was accidental.[34] We therefore fit the conductivity data for the partially hydrogenated bilayer, with the same expression as that for partially hydrogenated monolayer graphene, as shown in Figure 5b and c. The estimated value of n_i for samples B1 and B2 is 1.11×10^{13}/cm^2 and 1.26×10^{13}/cm^2, respectively, and the values for width of voltage plateau are 31.2 and 32.4 V, respectively. This impurity density value is significantly higher than the values estimated for pristine bilayer graphene ($\sim 4 \times 10^{10}$/cm^2).[32] These results are not surprising since the Raman data also support a comparable (or even higher) rate of hydrogenation for bilayer graphene in comparison to monolayer graphene. We however do not rule out the possibility that the above fit overestimates the impurity density for bilayer graphene, given the limited range of data available. More experiments are needed to clarify the exact impurity density and carrier density at which the transition from linear to sublinear behavior happens.

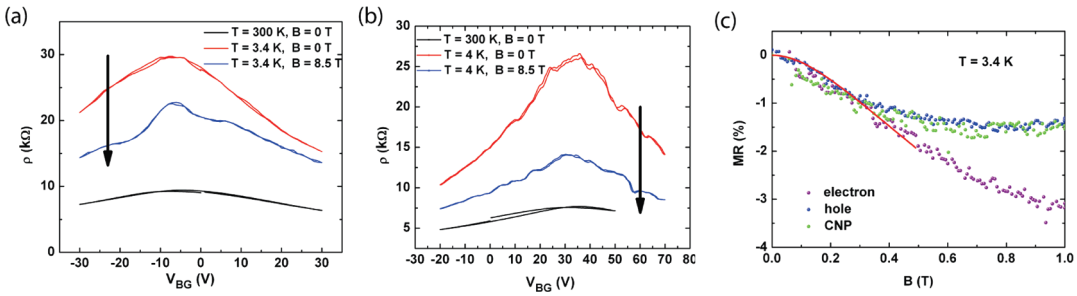

Figure 6. Low-temperature magnetotransport in partially hydrogenated bilayer graphene. (a) Resistivity (ρ) *vs* V_{BG} for: $T = 300$ K, zero-field (black); $T = 3.4$ K, zero-field (red); $T = 3.4$ K, $B = 8.5$ T (blue) for sample B2; (b) ρ *vs* V_{BG} for $T = 300$ K, zero-field (black); $T = 4$ K, zero-field (red); $T = 4$ K, $B = 8.5$ T (blue) for sample B1; and (c) MR (%) *vs* field at $T = 3.4$ K for sample B3, measured at charge neutrality point (green), $V_{CNP} + 30$ V (purple) and $V_{CNP} - 30$ V (blue). Red line is a fit to weak localization MR in the range 0−0.5 T.

We finally examine the transport properties of partially hydrogenated graphene under a magnetic field. Previous investigations on heavily hydrogenated[3] and ozonated[29] monolayer graphene have demonstrated the suppression of magnetoconductance oscillations. In the present work, we describe the magnetotransport in partially hydrogenated bilayer graphene samples (t = 10 s). A negative magnetoresistance (MR) is observed at low field ($B < 1$ T) for all densities (V_{BG} = CNP, CNP ± 30 V), as shown in Figure 6c for one sample (see Supporting Information, S8, for additional data). Considering the temperature dependence of resistivity discussed above, we analyze this negative MR within the framework of weak localization. Assigning the measured momentum scattering time equal to the intervalley scattering time, a weak localization fit to the low-field ($B < 0.5$ T) MR data[29,35] gives a phase coherence length $L_\varphi \sim 32$ nm at $T = 3.4$ K away from the neutrality point (V_{BG} = CNP ± 30 V), for sample B3 (see Supporting Information for details of fitting procedure). While this represents a typical value, some variations in the extent of negative MR are observed across different samples (see Supporting Information, S7). The negative MR also persists at high-magnetic fields, where its value at CNP is rather large (up to −46% at 8.5 T), as shown in Figure 6a and b. The characteristic magnetoconductance oscillations associated with quantum Hall effect in a 2DEG are notably suppressed in one sample (B1), and while remnants of quantization are barely present in the other sample (B2). This suppression of quantization effects implies a disorder length scale that is comparable to the magnetic length, $l_B = (\hbar/qB)^{1/2} \sim$ 8.6 nm (at $B = 8.5$ T). In principle, it may be possible to tune the electronic state of the system from an insulator to a quantum Hall conductor using magnetic field-induced delocalization, as was previously demonstrated in other 2DEG systems. However observing such physical phenomenon may require a precise control over the fraction of hydrogenated sites and also a much higher magnetic field.[36]

CONCLUSION

To summarize, it is shown that mobility changes in graphene are sensitive to the fraction of impurity atoms on the graphene plane. Changes in field-effect mobility can be used to estimate the extent of hydrogenation. Raman spectroscopy indicates linearly increasing defect-band intensity for increasing time exposure to hydrogenation, followed by a tendency to saturate. Charge transport, together with Raman spectroscopy allows a correlation of graphene mobility with the size of nanocrystalline regions formed upon incorporation of hydrogen atoms. For both mono- and bilayer graphene, the influence of hydrogen adatoms is consistent with their role as resonant scatterers that decrease mobility and induce midgap states. The formation of midgap states upon hydrogenation is reflected in the large width of voltage plateau. The temperature dependence of resistance for partially hydrogenated mono- and bilayer graphene indicates a weak insulating regime, particularly in the vicinity of the neutrality point which involves transport within these midgap states. Comparable rates for hydrogenation of mono- and bilayer graphene are obtained from both the evolution of defect peak in the Raman spectra and the density dependence of conductivity, indicating that bilayer graphene is also susceptible to hydrogenation despite a stiffer lattice.

METHODS

Fabrication and Electrical Measurement of Graphene FETs. Graphene flakes were prepared by micromechanical cleavage of graphite on Si/SiO_2 (300 nm) substrate. An 100 μL 4% polymethylmethacrylate (PMMA) (MicroChem, MW: 495 K) anisole solution was spin coated on substrates at 4000 rpm and baked at 180 °C for 2 min. The location of selected flakes is determined by defining optical markers on the PMMA. Source drain electrodes are patterned by electron beam lithography (FEI/Sirion), and this is followed by the development of PMMA with a methyl isobutyl

ketone (MIBK) and isopropyl alcohol (1:1) solution. Thermal evaporation of 5 nm Cr/30 nm Au is followed by lift off in warm acetone. For the fabrication of GNRs of 100 nm width, PMMA resist is spin coated, and the etch pattern designed with electron beam lithography is exposed to 20 W, 20 sccm oxygen plasma (RIE NTI-2312) for 10 s after resist development. For typical electrical measurements, a low frequency ac (~13 Hz), 100 nA drive current is applied across the source drain (S/D) terminals from the internal oscillator output of Stanford SR830 lock-in amplifier, and a phase-sensitive detection of the ac voltage across the S/D terminals is done to measure the graphene resistance. Measurements are typically performed in a four-terminal mode, except for an isolated single nanoribbon which is in two-terminal configuration. Graphene contact resistances are also measured, and negligible changes are observed upon hydrogenation. The back-gate voltage is applied to the silicon gate using Keithley 6430 subfemtoamp sourcemeter, and the typical gate leakage does not exceed 1−1.5 nA. For low-temperature measurement, the sample is immersed in flow of cold helium gas in a Cryogenics variable-temperature cryostat equipped with a 9 T superconducting magnet. The magnetic field is perpendicular to the substrate plane.

Controlled Exposure to Hydrogen Plasma. For controlled hydrogenation, the device at ambient temperature is exposed to different time intervals of radio frequency (RF) hydrogen plasma (RF Plasma system 13.56 MHz, 300 W) in a custom-designed ultrahigh-vacuum (UHV) chamber pumped to 10^{-9} Torr vacuum. The chamber pressure during the formation of RF hydrogen plasma was 5×10^{-6} Torr.

Raman Spectroscopy. The Raman spectra were obtained with a WITEC CRM200 Raman system. The excitation source is 532.05 nm laser (2.33 eV) with laser power below 0.1 mW to avoid laser-induced heating. The laser spot size at focus was around 500 nm in diameter with a 100× objective lens (NA = 0.95). Spectral resolution is 4 cm^{-1}. All G- and D-mode features were adequately fitted with a Lorentzian component of the Voigt profiles.

Acknowledgment. The authors thank the support of Singapore National Research Foundation under NRF-CRP grant "Graphene Related Materials and Devices" R-143-000-360-281. B.O. also acknowledges support by the Singapore National Research Foundation under NRF RF award no. NRFRF2008-07, NUS SMF Award, and ONR Award and by NUS NanoCore.

Supporting Information Available: Comparison of hydrogenation in mono- and bilayer graphene with Raman spectroscopy, device structure, procedure for fitting negative MR, simulation of the effect of fringe fields on nanoribbons mobility, typical gate leakage currents, and additional transport data. This material is available free of charge *via* the Internet at http://pubs.acs.org.

REFERENCES AND NOTES

1. Loh, K. P.; Bao, Q.; Ang, P. K.; Yang, J. The Chemistry of Graphene. *J. Mater. Chem.* **2010,** *2010*, 2277–2289.
2. Sofo, J. O.; Chaudhari, A. S.; Barber, G. D. Graphane: A Two-Dimensional Hydrocarbon. *Phys. Rev. B: Condens. Matter Mater. Phys.* **2007,** *75*, 153401.
3. Elias, D. C.; Nair, R. R.; Mohiuddin, T. M. G.; Morozov, S. V.; Blake, P.; Halsall, M. P.; Ferrari, A. C.; Boukhvalov, D. W.; Katsnelson, M. I.; Geim, A. K.; Novoselov, K. S. Control of Graphene's Properties by Reversible Hydrogenation: Evidence for Graphane. *Science* **2009,** *323*, 610–613.
4. Yang, M.; Nurbawono, A.; Zhang, C.; Feng, Y. P. Ariando Two-Dimensional Graphene Superlattice Made with Partial Hydrogenation. *Appl. Phys. Lett.* **2010,** *96*, 193115.
5. Ni, X.; Liang, G.; Wang, J.-S.; Baowen, L. Disorder Enhances Thermoelectric Figure of Merit in Armchair Graphane Nanoribbons. *Appl. Phys. Lett.* **2009,** *95*, 192114.
6. Zhou, J.; Wang, Q.; Chen, X. S.; Kawazoe, Y.; Jena, P. Ferromagnetism in Semi-Hydrogenated Graphene Sheet. *Nano Lett.* **2009,** *9*, 3867–3870.
7. Soriano, D.; Munoz-Rojas, F.; Fernandez-Rossier, J.; Palacios, J. J. Hydrogenated Graphene Nanoribbons for Spintronics. *Phys. Rev. B: Condens. Matter Mater. Phys.* **2010,** *81*, 165409.
8. Samarakonn, D. K.; Wang, X.-Q. Tunable Band Gap in Hydrogenated Bilayer Graphene. *ACS Nano* **2010,** *4*, 4126–4130.
9. Savini, G.; Ferrari, A. C.; Giustino, F. First-Principles Prediction of Doped Graphane as a High-Temperature Electron-Phonon Superconductor. *Phys. Rev. Lett.* **2010,** *105*, 037002.
10. Neto, A. H. C.; Guinea, F. Impurity-Induced Spin-Orbit Coupling in Graphene. *Phys. Rev. Lett.* **2009,** *103*, 026804.
11. Bostwick, A.; McChensey, J. L.; Emtsev, K. V.; Seyller, T.; Horn, K.; Kevan, S. D.; Rotenberg, E. Quasiparticle Transformation During a Metal-Insulator Transition in Graphene. *Phys. Rev. Lett.* **2009,** *103*, 056404.
12. Adam, S.; Hwang, E. H.; Galitski, V. M.; Sarma, S. D. A Self-Consistent Theory for Graphene Transport. *Proc. Nat. Acad. Sci. U.S.A.* **2007,** *104*, 18392–18397.
13. Klos, J. W.; Zozoulenko, I. V. Effect of Short- and Long-range Scattering on the Conductivity of Graphene: Boltzmann Approach vs Tight-Binding Calculations. *Phys. Rev. B: Condens. Matter Mater. Phys.* **2010,** *82*, 081414(R).
14. Katsnelson, M. I.; Novoselov, K. S. Graphene: New Bridge Between Condensed Matter Physics and Quantum Electrodynamics. *Solid State Commun.* **2007,** *143*, 3–13.
15. Stauber, T.; Peres, N. M. R.; Guinea, F. Electronic Transport in Graphene: A Semiclassical Approach Including Midgap States. *Phys. Rev. B: Condens. Matter Mater. Phys.* **2007,** *76*, 205423.
16. Ni, Z. H.; Ponomarenko, L. A.; Nair, R. R.; Yang, R.; Anissimova, S.; Grigorieva, I. V.; Schedin, F.; Blake, P.; Shen, Z. X.; Hill, E. H.; Novoselov, K. S.; Geim, A. K. On Resonant Scatterers As a Factor Limiting Carrier Mobility in Graphene. *Nano Lett.* **2010,** *10*, 3868–3872.
17. Katoch, J.; Chen, J.-H.; Tsuchikawa, R.; Smith, C. W.; Mucciolo, E. R.; Ishigami, M. Uncovering the Dominant Scatterer in Graphene Sheets on SiO2. *Phys. Rev. B: Condens. Matter Mater. Phys.* **2010,** *82*, 081417(R).
18. Pachoud, A.; Jaiswal, M.; Ang, P. K.; Loh, K. P.; Özyilmaz, B. Graphene Transport at High Carrier Densities Using a Polymer Electrolyte Gate. *EPL* **2010,** *92*, 27001.
19. Ni, Z. H.; Wang, H. M.; Ma, Y.; Kasim, J.; Wu, Y. H.; Shen, Z. X. Tunable Stress and Controlled Thickness Modification in Graphene by Annealing. *ACS Nano* **2008,** *2*, 1033–1039.
20. Malard, L. M.; Pimentaa, M. A.; Dresselhaus, G.; Dresselhaus, M. S. Raman Spectroscopy in Graphene. *Phys. Rep.* **2009,** *473*, 51–87.
21. Tuinstra, F.; Koenig, J. L. Raman Spectrum of Graphite. *J. Chem. Phys.* **1970,** *53*, 1126–1130.
22. Sato, K.; Saito, R.; Oyama, Y.; Jiang, J.; Cancado, L. G.; Pimenta, M. A.; Jorio, A.; Samsonidze, G. G.; Dresselhaus, G.; Dresselhaus, M. S. D-Band Raman Intensity of Graphitic Materials as a Function of Laser Energy and Crystallite Size. *Chem. Phys. Lett.* **2006,** *427*, 117–121.
23. Chen, J.-H.; Cullen, W. G.; Jang, C.; Fuhrer, M. S.; Williams, E. D. Defect Scattering in Graphene. *Phys. Rev. Lett.* **2009,** *102*, 236805.
24. Ryu, S.; Han, M. Y.; Maultzsch, J.; Heinz, T. F.; Kim, P.; Steigerwald, M. L.; Brus, L. E. Reversible Basal Plane Hydrogenation of Graphene. *Nano Lett.* **2008,** *8*, 4597–4602.
25. Xiang, H.; Kan, E.; Wei, S.-H.; Whangbo, N.-H.; Yang, J. Narrow" Graphene Nanoribbons Made Easier by Partial Hydrogenation. *Nano Lett.* **2009,** *9*, 4025–4030.
26. Vasko, F. T.; Zozoulenko, I. V. Conductivity of a Graphene Strip: Width and Gate-Voltage Dependencies. *Appl. Phys. Lett.* **2010,** *97*, 092115.
27. Bang, J.; Chang, K. J. Localization and One-Parameter Scaling in Hydrogenated Graphene. *Phys. Rev. B: Condens. Matter Mater. Phys.* **2010,** *81*, 193412.
28. Morozov, S. V.; Novoselov, K. S.; Katsnelson, M. I.; Schedin, F.; Elias, D. C.; Jaszczak, J. A.; Geim, A. K. Giant Intrinsic Carrier Mobilities in Graphene and Its Bilayer. *Phys. Rev. Lett.* **2008,** *100*, 016602.
29. Moser, J.; Tao, H.; Roche, S.; Alsina, F.; Torres, C. M. S.; Bachtold, A. Magnetotransport in Disordered Graphene Exposed to Ozone: From Weak to Strong Localization.

Phys. Rev. B: Condens. Matter Mater. Phys. **2010,** *81*, 205445.
30. Zabrodskii, A. G. The Coulomb Gap: the View of the Experimenter. *Philos. Mag. B* **2001,** *81*, 1131.
31. Jaiswal, M.; Wang, W.; Fernando, K. A. S.; Sun, Y.-P.; Menon, R. Magnetotransport in Transparent Single-Wall Carbon Nanotube Networks. *Phys. Rev. B: Condens. Matter Mater. Phys.* **2007,** *76*, 113401.
32. Ferreira, A.; Gomes, J. V.; Nilsson, J.; Mucciolo, E. R.; Peres, N. M. R.; Neto, A. H. C. A Unified Description of the DC Conductivity of Monolayer and Bilayer Graphene Based on Resonant Scatterers; 1010.4026v1, 2010.
33. Yuan, S.; Raedt, H. D.; Katsnelson, M. I. Electronic Transport in Disordered Bilayer and Trilayer Graphene. *Phys. Rev. B: Condens. Matter Mater. Phys.* **2010,** *82*, 235−409.
34. Monteverde, M.; Ojeda-Aristizabal, C.; Weil, R.; Bennaceur, K.; Ferrier, M.; Guéron, S.; Glattli, C.; Bouchiat, H.; Fuchs, J. N.; Maslov, D. L. Transport and Elastic Scattering Times as Probes of the Nature of Impurity Scattering in Single-Layer and Bilayer Graphene. *Phys. Rev. Lett.* **2010,** *104*, 126801.
35. McCann, E.; Kechedzhi, K.; Fal'ko, V. I.; Suzuura, H.; Ando, T.; Altshuler, B. L. Weak-Localization Magnetoresistance and Valley Symmetry in Graphene. *Phys. Rev. Lett.* **2006,** *97*, 146805.
36. Jiang, H. W.; Johnson, C. E.; Wang, K. L.; Hannahs, S. T. Observation of Magnetic-Field-Induced Delocalization: Transition from Anderson Insulator to Quantum Hall Conductor. *Phys. Rev. Lett.* **1993,** *71*, 1439–1442.